Shape Analysis of the Peripapillary RPE Layer in Papilledema and Ischemic Optic Neuropathy

Patrick Sibony,[1,2] *Mark J. Kupersmith,*[3,4] *and F. James Rohlf*[5]

Purpose. Geometric morphometrics (GM) was used to analyze the shape of the peripapillary retinal pigment epithelium–Bruch's membrane (RPE/BM) layer imaged on the SD-OCT 5-line raster in normal subjects and in patients with papilledema and ischemic optic neuropathy.

Methods. Three groups of subjects were compared: 30 normals, 20 with anterior ischemic optic neuropathy (AION), and 25 with papilledema and intracranial hypertension. Twenty equidistant semilandmarks were digitized on OCT images of the RPE/BM layer spanning 2500 μm on each side of the neural canal opening (NCO). The data were analyzed using standard GM techniques, including a generalized least-squares Procrustes superimposition, principal component analysis, thin-plate spline (to visualize deformations), and permutation statistical analysis to evaluate differences in shape variables.

Results. The RPE/BM layer in normals and AION have a characteristic V shape pointing away from the vitreous; the RPE/BM layer in papilledema has an inverted U shape, skewed nasally inward toward the vitreous. The differences were statistically significant. There was no significant difference in shapes between normals and AION. Pre- and posttreatment OCTs, in select cases of papilledema, showed that the inverted U-shaped RPE/BM moved posteriorly into a normal V shape as the papilledema resolved with weight loss or shunting.

Conclusions. The shape difference in papilledema, absent in AION, cannot be explained by disc edema alone. The difference is a consequence of both the translaminar pressure gradient and the material properties of the peripapillary sclera. GM offers a novel way of statistically assessing shape differences of the peripapillary optic nerve head. (*Invest Ophthalmol Vis Sci.* 2011;52:7987–7995) DOI:10.1167/iovs.11-7918

The ability of spectral-domain optical coherence tomography (SD-OCT) to measure the thickness of the retinal nerve fiber layer (RNFL) is a useful method of assessing the structure of the optic disc in glaucoma and other optic neuropathies.[1–6] The SD-OCT has also been used in the diagnosis and management of disc edema by quantifying a peripapillary circular tomogram of retinal nerve fiber thickness.[7–10] Scott et al.[11] have validated the RNFL thickness to assess the degree of disc edema by correlating it with fundus photographs. The application of the SD-OCT to evaluate subsurface architecture of the optic disc has primarily been used to study experimental glaucoma.[12,13] We recently reported[14] that some patients with papilledema will exhibit inward angulation of the peripapillary retinal pigment epithelium–basement membrane (RPE/BM) layer imaged on the horizontal axial 5-line raster taken through the optic nerve head. We observed qualitative changes in the shape of the RPE/BM layer after treatment with shunting surgery or weight loss. We also measured the angular deviation of the RPE margin from a peripheral, presumably normal reference plane of the RPE layer. Although the angulation was apparent on the raster images in many patients, approximately 40% of patients failed to show any deformation of the RPE/BM layer. However, in some cases, determination of the reference plane was difficult to establish. The impetus for this study was to find a more precise way of characterizing this deformation.

Geometric morphometrics (GM) is an analytic technique originally developed to quantify and statistically assess variation in the *shape* of biological forms and their covariation with other variables.[15–17] This methodology defines shape as the geometric properties of a form that remains after filtering out variations due to differences in position, scale, and orientation. Sanfilippo et al.[17] have recently proposed that this analytic technique may have applications in ophthalmology and have used GM to analyze the shape of the optic cup in glaucoma.[18] The purpose of the present study was to evaluate the application of GM to analyze the shape of the peripapillary RPE/BM layer in patients with papilledema and ischemic optic neuropathy. This technique may bring new insights into the biomechanics of the optic disc in patients with intracranial hypertension and expand the morphometric toolbox used to assess the optic disc.

Methods

We will provide an overview of the basic principles of GM and describe how we applied the methodology in our study. The technical details are described more fully in the introductory monograph on GM by Zelditch et al.[15] Although the computations are complex, there is reliable and accessible software that can be downloaded from several web sites. The Geometric Morphometric Web Site maintained by one of us (FJR) at SUNY Stony Brook has a comprehensive list of programs, associated links,[19] and downloadable versions of the TPS series, which is the industry standard. The software we used in this study relied primarily on tpsRelw, tpsDig2, tpsUtil, and tpsRegr by FJR. Where indicated below, we also used software from the Integrated Morphometrics Package (IMP) by H. David Sheets.[20]

Image Acquisition

SD-OCT scans were acquired with an SD-OCT (Cirrus; Carl Zeiss Meditec, Inc, Dublin, CA). Sharply focused, uniformly illuminated images

From the Departments of [1]Ophthalmology and [5]Ecology and Evolution, and the [2]SUNY Eye Institute, University Hospital Medical Center, State University of New York, Stony Brook, New York; and the [3]Hyman-Newman Institute for Neurosurgery, St. Luke's-Roosevelt Hospital, New York, New York; and the [4]New York Eye and Ear Infirmary, New York, New York.

Supported by National Eye Institute Grants U10 EY017281-01A1 and U10 EY017281-01A1S1 and in part by an unrestricted departmental educational research grant from Davis Optical.

Submitted for publication May 21, 2011; revised August 14, 2011; accepted August 26, 2011.

Disclosure: **P. Sibony**, None; **M.J. Kupersmith**, None; **F.J. Rohlf**, None

Corresponding author: Patrick Sibony, Department of Ophthalmology, Health Sciences Center, University Hospital and Medical Center, State University of New York, Stony Brook, NY 11794; patrick.sibony@sbumed.org.

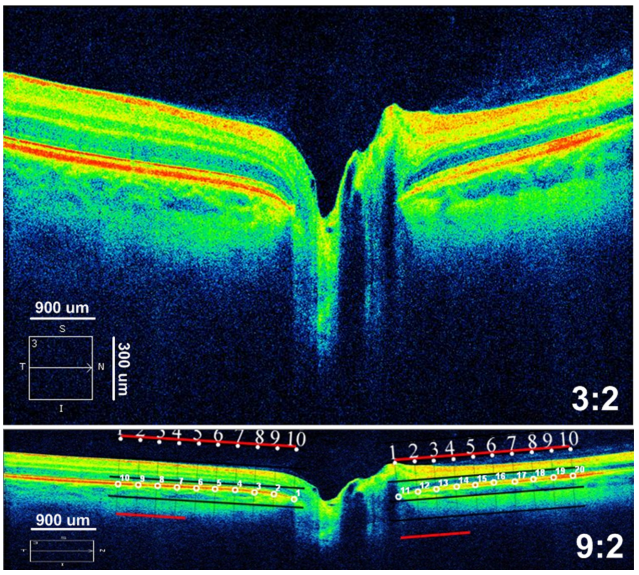

FIGURE 1. Axial SD-OCT 5-line raster scan displayed with an aspect ratio of 3:2 (*top*) and 9:2 (*bottom*). The 3:2 image magnifies the vertical scale, to enhance viewing of the retinal layers. The image is decreased with image-analysis software (Photoshop; Adobe Systems, Inc., San Jose, CA) along the vertical dimension to one third its height to equalize the both horizontal and vertical dimensions. *Bottom inset*: placement of semilandmarks (*small*, *numbered circles*) by superimposing a 2500-μm grid on the temporal (points 1–10) and nasal (points 11–20) side of the NCO after adjusting the aspect ratio. Note that the image is centered, flat, and symmetrical and that the grid is positioned parallel to the RPE/BM layer at the NCO.

centered over the optic nerve head were obtained using two standard protocols: (1) optic disc cube 200 × 200 and (2) a 5-line, horizontal, high-definition raster (9 mm long, 0.25-mm intervals). The raster scan was positioned through the central portion of the optic disc with signal strength of ≥7. Images were saved in the highest quality .jpg format, producing an image of 750 × 500 pixels. For a 9-mm, 5-line raster scan, the vertical dimension was reduced to one third of its height because the displayed image on the SD-OCT is vertically magnified to highlight the retinal layers (Fig. 1). To more accurately assess the image, we converted the display aspect ratio from 3:2 to a true aspect ratio of 9:2 (750 × 167 pixels), which provides a uniform scale along both vertical and horizontal dimensions.

In some cases, the axial image on the 5-line raster may appear tilted, as shown in Figure 2. This is a parallax artifact that occurs when the scan beam is obliquely positioned, usually over the nasal or central region of the pupil. If the scan beam is positioned over the temporal portion of the pupil, the beam will be perpendicularly oriented over the optic nerve so that the image is symmetrical and untilted (Fig. 2a). The actual position of the scan beam through the pupil that is necessary to obtain an untilted image may vary, depending on the refractive error (and presumably the axial length and shape) of the posterior pole. The parallax artifact may affect the shape of the posterior pole, especially when comparing the shape at different levels of the posterior pole on the OCT (e.g., the disc surface to RPE/BM). To minimize this artifact and to ensure consistency between subjects, we used only untilted images where the disc was centered and the tilt did not exceed 10° on the uncorrected 3:2 aspect image.

Subjects

The images were obtained retrospectively from a departmental SD-OCT database and medical records. The images included one eye each from 75 subjects: 25 with papilledema and intracranial hypertension, 20 with nonarteritic anterior ischemic optic neuropathy (AION), and 30 with clinically normal optic discs. The right eye was used in all subjects with papilledema and normals. If the left eye was affected in subjects with AION, the image was flipped horizontally to align the temporal and nasal regions across all subjects. The diagnosis of papilledema was based on generally accepted clinical funduscopic features, including elevation, blurring of the margins, vascular engorgement, circumpapillary folds, and hemorrhages. All subjects with papilledema had opening pressures of >250 mm water and SD-OCT evidence of average RNFL thickening (>95% of the normal controls, by Cirrus HD SD-OCT,). Twenty-three of the papilledema subjects had idiopathic intracranial hypertension (21 women, 2 men): One patient had a venous sinus thrombosis and the other a large frontal lobe meningioma. Among subjects with normal optic discs, we excluded those with clinically abnormal acuity, color vision, pupillary findings, intraocular pressure, visual fields, and ophthalmoscopic findings or SD-OCT evidence of an optic neuropathy, optic atrophy, glaucoma or congenital disc anomalies (e.g., drusen, hypoplasia, oblique insertion, tilting, high myopia, staphylomas or otherwise dysplastic). This study was approved by the SUNY Stony Brook Committee on Research Involving Human Subjects and complied with the Declaration of Helsinki.

Digitizing Structural Semilandmarks

Image-analysis software (Photoshop; Adobe Systems, San Jose, CA) was used to superimpose a transparent line grid spanning 2500 μm on either side of the neural canal opening (NCO; Fig. 1b). The grid was positioned parallel to the flattest portion of the RPE/BM on both sides of the NCO, with a starting reference point positioned at the innermost termination of the RPE/BM layer (see white line placement in Fig. 6). The grid was used to position 10 points (slightly less than 278 μm

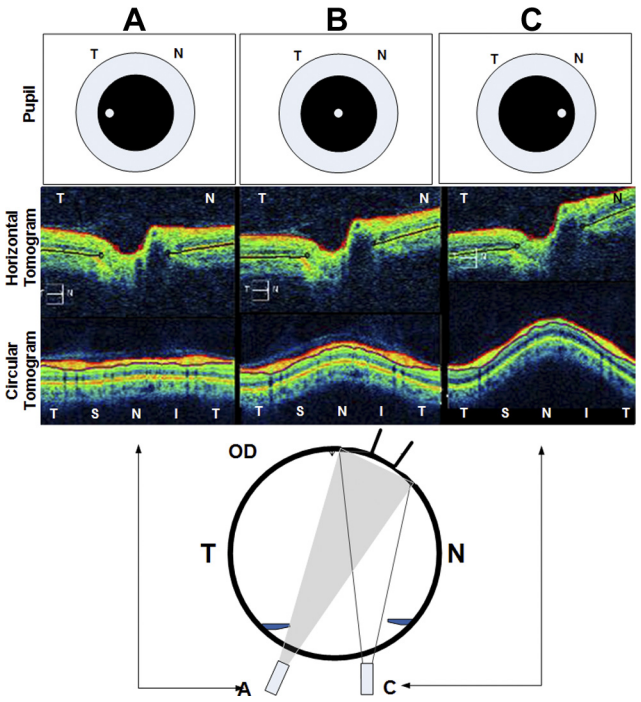

FIGURE 2. The parallax artifact of the OCT in the right eye of a normal subject. *Top row*: location of the scanning beam on the pupil. The corresponding horizontal (*second row*) and circular (*third row*) tomograms are shown. When the aiming beam is located over the nasal region of the pupil in an emmetropic patient, the image is tilted (as in column C). To obtain a symmetrical untilted view of the disc and peripapillary region the beam must scan perpendicular to the target (column A). When the scanning beam is obliquely oriented (C, *bottom inset*), the echo delay of the nasal retina is shorter than the temporal retina, causing the image to tilt. The degree of tilting relative to beam location on the pupil may vary with the axial length, refractive error, and shape of the eye. T, temporal; N, nasal.

apart) along the posterior surface of the RPE/BM layer on the temporal and nasal side of the NCO. Points 1 to 10 were placed temporally and 11 to 20 nasally. FJR's tpsUtil and tpsDig2 software[19] was used to digitize the semilandmarks and generate .tps text files for analysis. All shape figures depict the nasal RPE on the right side of the image; the temporal RPE is located on the left side.

The use of a fixed-length transparent straight line grid might in some cases demarcate a slightly longer linear distance on a steeply curved shape than a flat shape. To minimize this effect, we excluded subjects with high myopia or staphylomas, in which the relative curvature of the posterior pole can be extreme. We compared the distance measured by using a straight grid, as in Figure 1, with the measurement of equidistant points precisely contoured along the path of the RPE in 10 subjects with papilledema and 10 normals. We found that the difference [(contoured length − straight grid length)/straight grid length], on average, was less than 1% (0.58% normals, 0.86% papilledema). A permutation statistical comparison showed no significant difference between these two methods of semilandmark placement.

These points are called semilandmark rather than landmark points because, with the exception of points 1 and 11 located at the NCO border, their locations do not correspond to unique morphologic landmarks.[21] They are simply positioned at equidistant points starting at the NCO to capture the shape of the RPE/BM complex. However, for simplicity, they were treated as landmarks in the present study, because the special adjustments for semilandmark points available in GM made little difference in the results.

Reliability of the placement of the semilandmark points on the outer border of the RPE/BM was assessed by obtaining two sets of 5-line rasters from two subjects, same eye, five times, on two separate days. Both sets of data were tested for shape differences using permutation statistics. We found no statistically significant difference between the two sets of data. Thin-plate spline comparisons failed to show any appreciable differences between any of the digitized semilandmarks for each subject.

We also measured the NCO directly from the nasal to the temporal edge of the RPE/BM (Digimizer; MedCalc Software, ver. 3.7, 2005–2009l MedCalc, Mariakerke, Belgium; www.digimizer.com) image-analysis software. Average RNFL thickness was obtained from the standard optic nerve head analysis report of the Cirrus SD-OCT.

Generalized Least-Squares Procrustes Superimposition

Generalized least-squares (GLS) Procrustes superimposition is the iterative process of estimating a mean shape and then superimposing all the objects onto this mean shape. This process is performed in three steps.[15] First, the set of points for each subject is adjusted so that their centroid (mean of all the x coordinates, mean of all the y coordinates) is translated to the origin by subtracting centroid coordinates from the coordinates of each landmark. Second, each configuration is scaled by dividing by centroid size (the square root of the summed squared distances of each landmark from the centroid of its landmark configuration). Third, rotational differences are removed by iteratively minimizing the summed squared distances between corresponding landmarks.

Thin-Plate Spline

The thin-plate spline has two important functions. First, it is used to depict shape differences as a smooth deformation of one shape into another using an algorithm that interpolates potential changes between landmarks of a reference shape (usually the mean shape), and the shape it is being compared with. These same shape differences can also be visualized using vectors at each landmark showing the magnitude and direction of the differences at each landmark.

The thin plate spline is also used to define a set of shape variables, partial warps that capture the shape differences among the objects being compared. The partial warp scores provide data matrices that can be analyzed with conventional multivariate statistical methods.

Principal Component Analysis

Because shape variation is multidimensional, principal components analysis (PCA) was used to express as much of the variation as possible in just a few dimensions that are linear combinations of the partial warps. This allows one to identify and display most of the variation in shape between subjects. The relative contribution of each dimension is proportional to its variance. The tpsRelW software was used for these computations.

Canonical variant analysis (CVA) is analogous to PCA. Whereas PCA is used to describe differences among subjects, CVA is designed to describe differences between group means relative to variation found within the groups. It is thus useful for discrimination between groups. We used the IMP program CVAGen6j (ver. 5-13-03).

Statistical Analysis

A test statistic adapted to assessing shape differences was proposed by Goodall.[22] It compares sums of squared Procrustes differences between and within the samples being compared and expresses it as an F ratio. Although his original proposal to compare his F statistic to the usual F distribution is usually not valid due to restrictive assumptions, valid statistical tests can usually be made by comparing the observed F value to an empiric distribution based on a large number (10,000 in the present study) of random permutations of the assignments of individuals to the groups being compared. The proportion of Goodall's F statistics from permuted data sets that are equal to or larger than the observed Goodall's statistic is interpreted as the probability value for the test. Goodall's F-test considers only the total amount of shape variation and does not tell one what the differences are.

For traditional morphometric measurements (e.g., disc elevation, average RNFL, and NCO diameters), we used Student's t-test and ANOVA where appropriate.

Results

The average RNFL thickness in papilledema was 241 μm (SD 112; range, 124–495), AION was 209 μm (SD 82 μm; range, 107–357), and normals was 92 μm (SD 10; range, 90–119). There was no significant difference in average RNFL thickness between papilledema and AION. The differences between normals and papilledema and between normals and AION are statistically significant (ANOVA, $P < 0.001$ for each).

A generalized Procrustes superimposition of 20 semilandmarks in all 75 subjects that included 30 normal optic discs [red], 25 papilledema [blue], and 20 AION [black]) is shown in the scatterplot in Figure 3a. The consensus or mean shapes of the Procrustes transformed semilandmarks for each group are shown in Figures 3b and 3c illustrating the differences in the shape of the peripapillary RPE/BM in normals, AION, and papilledema. The magnitude and direction of the difference between papilledema and normals from the consensus is shown in a vector plot that is vertically expanded threefold as it would appear on commercial displays, with a 3:2 aspect ratio (Fig. 3d). These plots all demonstrate that the mean RPE/BM layer in normals and in AION has a V-shaped configuration sloped outwardly (away from the vitreous) as it approaches its central margin at the NCO. In contrast, subjects with papilledema have an inverted U-shaped RPE/BM layer that is anteriorly displaced toward the vitreous. There is a slight nasal skew in the inverted U shape compared with the relatively symmetrical V shape in normals.

A variance–covariance matrix of the shape variables derived from the semilandmark data from all three groups was used to perform a principal component analysis (using tpsRelW soft-

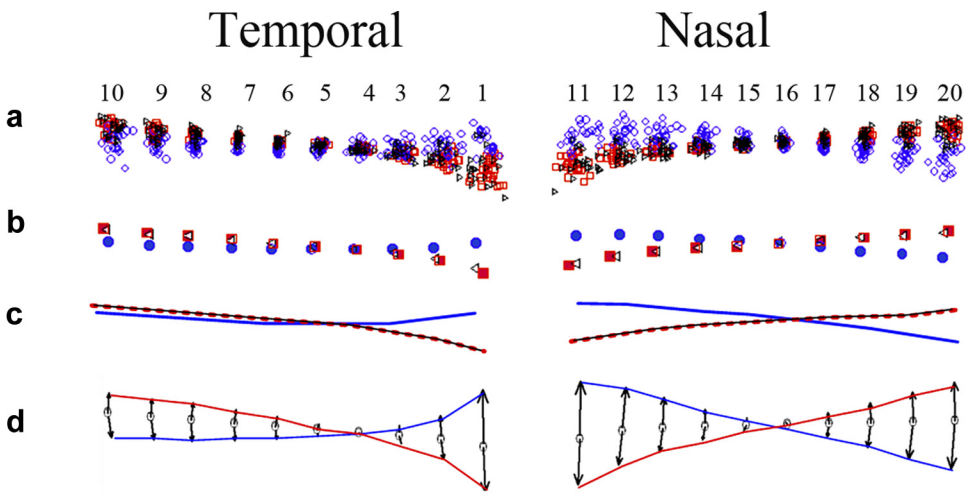

FIGURE 3. (**a**) Procrustes superimposition of 20 semilandmarks from 75 optic discs. The semilandmark scatter from each group is color coded: *Blue*, papilledema; *red*, normals; *black*, AION. (**b**) Consensus or mean shape from each group of patients. (**c**) Line tracing of semilandmarks shown in (**b**). (**d**) Threefold vertical expansion to emphasize difference and exhibit the mean shape differences as they would be appear on commercial displays with a 3:2 aspect ratio. The last figure compares papilledema to normals (excludes AION). All these plots demonstrate that the RPE/BM layer in patients with papilledema have an asymmetric inverted U shape that is inwardly bowed toward the vitreous and slightly skewed nasally. Those with AION and normals have a relatively symmetrical V-shaped RPE/BM. Analysis and plots were generated using tpsRelw v1.37 (FJR, Stony Brook, NY) and IMP PCAGen6j software.

ware[19]). The first two principal components together account for 88% of the variance; 63% from PC1 alone. Figure 4a shows the distribution of principal component scores from each subject along the first two PC axes. The shape implied along the PC1 axis depicts a deformation that ranges from an inverted U (on the negative abscissa) to a V shape (on the positive abscissa; Fig. 4b). The PC2 on the ordinate describes a shape change that goes from NCO contraction (up–in) on the positive side and NCO expansion (down–out) on the negative side (Fig. 4c). The intersection of PC1 and PC2 represents the consensus shape of the RPE/BM semilandmarks in all the specimens. The PC plot shows two distinct clusters (papilledema versus normals). With one exception, nearly all subjects with papilledema exhibited some degree of the inverted U-shaped deformation or relative flattening (to the consensus) not typically seen in normals. The probability that this difference in shape between papilledema and normal subjects could have arisen by chance was 1 in 10,000 permuted data or $P = 0.0001$ and thus significant.

The Procrustes scatterplot and thin-plate spline vector plots failed to demonstrate any appreciable differences in shape between AION and normals. Like normals, most of the subjects with AION exhibited a flat or V-shaped configuration. There was considerable overlap with normals and very little overlap with papilledema along PC1.

These findings were confirmed with a canonical variate analysis (CVA) on the entire group of subjects, showing that there was only one distinguishable group: papilledema. We were unable to distinguish AION from normals as a distinct canonical group, at least in this sample size. In addition, there was a significant difference between AION and papilledema (permutation $P = 0.0001$).

When the thin-plate spline was used to visualize the results of the PCA, there appeared to be a very slight increase in the relative distance between semilandmarks 1 and 11 among eyes with AION, which suggests a small radial expansion of the NCO relative to the overall shape. The difference in shape between AION and normals exhibited a slight trend toward expansion, but was not statistically significant (permutation $P = 0.06$). To further explore this observation, we assessed the NCO by measuring the horizontal diameter directly on the same set of images for each group (AION, papilledema, and normals) and also included the unaffected eye in those subjects with AION. The results are shown in Figure 5. ANOVA failed to show significant differences between any of the groups.

We used a generalized form of Goodall's F statistic to test whether shape is a linear function of RNFL. We found no significant association when using permutation statistical analysis for any of the groups we studied: normals ($P = 0.36$, accounted for only 4% of the sum of the squared Procrustes distance), AION ($P = 0.41$, 5% of the variation accounted for), and papilledema ($P = 0.13$, 8% accounted for).

The shape differences described above are clinically illustrated in the two cases with papilledema shown in Figures 6 and 7. Both cases had indentation of the globe, with an anteriorly displaced, inward, U-shaped deformation of the RPE/BM layer. The first case demonstrates the rapidity with which this deformation can revert to normal after a lumbar puncture. It also demonstrates the shadowing of the RPE/BM that is frequently seen in subjects with severe disc edema and how the NCO can be identified, even in cases with significant shadowing. The second case compares the deformation on SD-OCT, using the standard display and corrected aspect ratios with corresponding flattening of the globe on MRI typically seen in subjects with intracranial hypertension.[23,24]

DISCUSSION

The capacity of commercial 870-nm wavelength SD-OCTs to image the sclera and lamina cribrosa is limited by its depth of penetration. The RPE/BM layer, however, can be visualized, even with significant disc edema (Fig. 6). Although surface deformations may not always reflect deformations at a deeper level with increased intraocular pressure,[25,26] we suggest that in the absence of sub-RPE fluid, the RPE/BM approximates the deformations of the load bearing sclera and thus may provide insights into the biomechanics of the nerve head in papill-

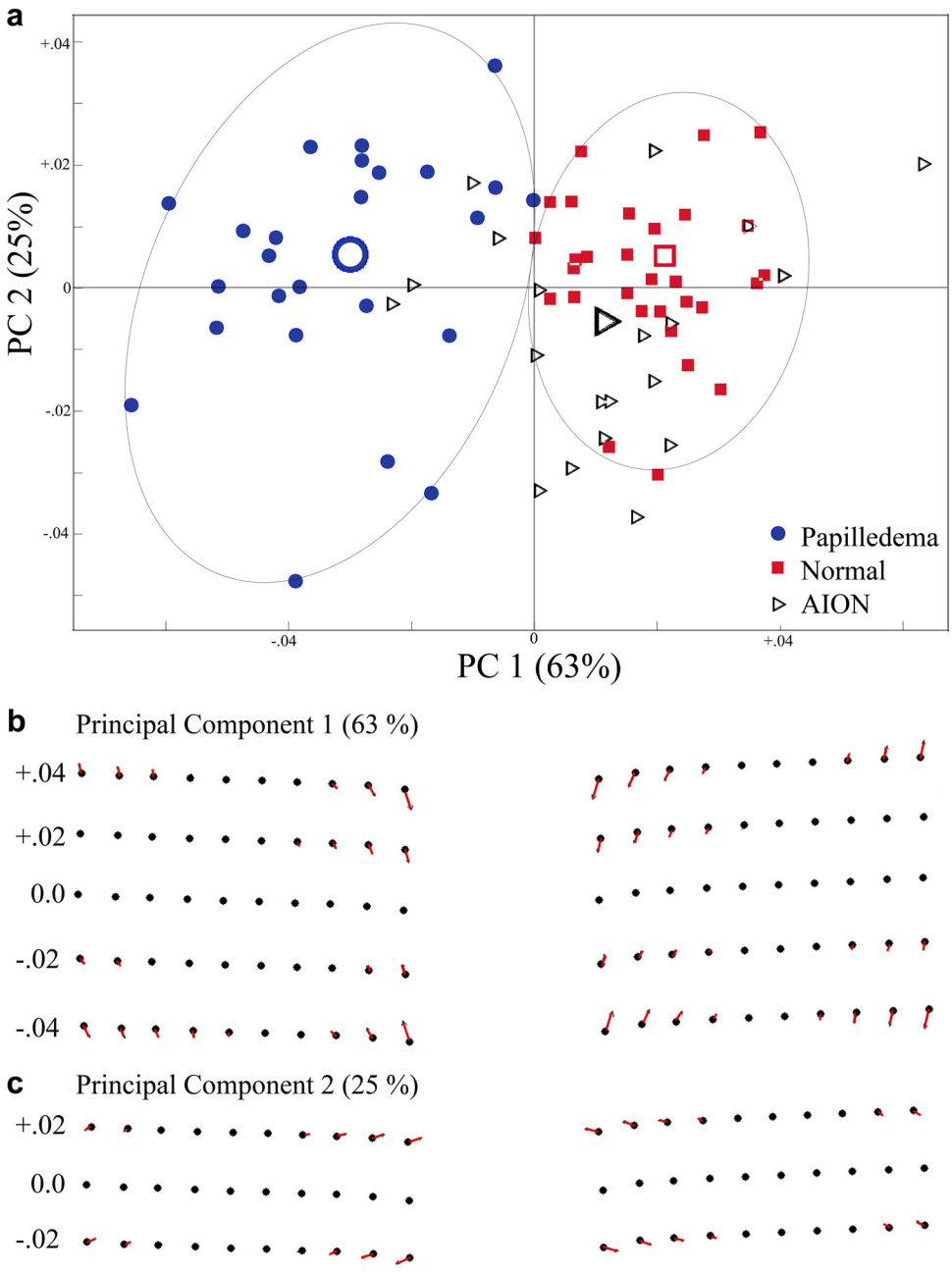

FIGURE 4. The first two dimensions of a PCA for PC1 versus PC2. (**b**, **c**) The shapes implied by each respective principal component along PC1 and PC2 relative to the consensus (*black dots*). Most of the shape variation (63%) is depicted along PC1, which describes an inward-bowing U shape on the negative side of the abscissa to a mild V shape on the positive side. PC2 responsible for 25% of the variance depicts a shape deformation that goes from expansion of the NCO (negative ordinate) to contraction of the NCO (positive ordinate). The principal component score for each patient is plotted relative to their position along each of these PCs. The large open icons represent the mean PC score from each group. Note that the patients with papilledema are distinctly clustered from the normals. AION patients show some overlap but are clearly more like normals than papilledema. The difference between papilledema and normal/AION was statistically significant.

edema. Technological advances in the SD-OCT using enhanced-depth imaging or high-wavelength source (1050-nm) should, in the near future, overcome this depth limitation[27,28] enough to visualize the sclera and lamina cribrosa.

There were distinctive shape characteristics of the peripapillary RPE/BM among the subjects with intracranial hypertension compared with normals and AION. The temporal–nasal peripapillary RPE/BM of the normal optic disc had a characteristic V shape, bowed posteriorly away from the vitreous, that gently steepened as it approached the NCO (Fig. 3). This shape had a narrow range from a relatively flat V shape to one that was slightly steeper. In contrast, the temporal–nasal RPE/BM in subjects with papilledema had an inverted U shape that gently bent anteriorly and skewed nasally toward the vitreous. Furthermore, the difference in shape between papilledema and normals was not associated with any measurable change in the horizontal diameter of the NCO.

We compared AION to papilledema to determine whether disc edema alone affects the shape of the RPE/BM. We found that the inverted U shape in papilledema was not explained by the presence of disc edema alone, because the degree of disc edema, based on the average RNFL thickness, in AION and papilledema was the same. In addition, the V-shaped RPE/BM in AION was statistically indistinguishable from normals and significantly different from the shape in papilledema.

The shape differences in the RPE/BM layer demonstrated in this study were consistent with both experimental and clinical observations. Using confocal scanning laser tomography in dogs, Morgan et al.[29,30] showed that intracranial hypertension displaces the optic disc surface anteriorly (toward the vitreous) whereas ocular hypertension displaces the disc surface posteriorly. The indentation of the globe visualized on the SD-OCT as an inverted U shape is a quantifiable, high-resolution image of the flattening of the posterior globe that has been described

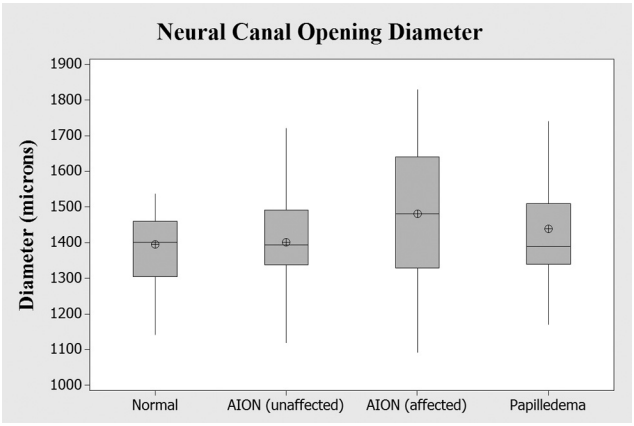

FIGURE 5. The horizontal diameter of the NCO in three groups of patients: normals, papilledema, and AION (affected and unaffected eye). Lengths were measured directly. The slight relative expansion of the NCO exhibited on the thin-plate spline and the mild differences implied along PC2 among patients with AION was not statistically significant by ANOVA. Box-whisker plots indicate interquartile range (25th–75th percentile), median (*line*), mean (*cross hair*), and range (*whiskers*).

on the orbital MRI, CT scan, and B scan in patients with intracranial hypertension (Fig. 7).[24,31–34] Flattening of the globe has also been observed in subjects with (1) papilledema with choroidal folds,[35,36] (2) choroidal folds with intracranial hypertension in the absence of papilledema,[36] and (3) idiopathic choroidal folds (where intracranial pressure was found to be normal),[33,35,37] (4) hypotony,[38] and (5) optic nerve sheath meningiomas.[39] Flattening of the globe can cause a measurable decrease in axial length[40] and an acquired hyperopia.[41] We anticipate that a GM analysis of the RPE/BM using SD-OCT in some subjects with choroidal folds, hypotony, and meningiomas will exhibit similar shape changes as in the papilledema described in this study.

Based on a proportionate comparison of the consensus shapes in each group, we estimate that there is approximately a 100- to 300-μm difference in the relative position of the RPE/BM at the NCO between normals and papilledema. The patient shown in Figure 6 exhibited a relative posterior displacement of the RPE/BM at its margin after the LP and treatment of approximately 150 to 250 μm. The signature case used in our previous report[14] showed a displacement of 200 to 300 μm after treatment. There are, however, patients who show very little change in shape, even after treatment and resolution of the disc edema. Patients with papilledema, choroidal folds due to intracranial hypertension with or without papilledema, and idiopathic choroidal folds may exhibit hyperopic shifts of approximately +1.00 to +2.00 D,[32,36,37] sometimes more.[42] A 1-mm (1000-μm) shift in axial length is approximately equal to +3.00 D of hyperopia. The magnitude of RPE/BM displacement in papilledema that we observed is consistent with reported range of acquired hyperopia in patients with papilledema. This degree of anterior displacement probably also explains the refractive scotoma that enlarges the blind spot in papilledema.[43]

By comparison, the magnitude of displacements of the lamina or disc surface that occur in experimental glaucoma are on the order of 10 to 80 μm.[44–46] Morgan et al.[29] showed that, in dogs, small areas of the optic disc surface can move more than 128 μm in response to elevation of the IOP. They noted that small increases in cerebral spinal fluid pressure have a greater effect than equivalent increases in IOP and that most of the movement occurs at lower pressures. Yang et al.[47] showed that posterior laminar displacement in experimental glaucoma may

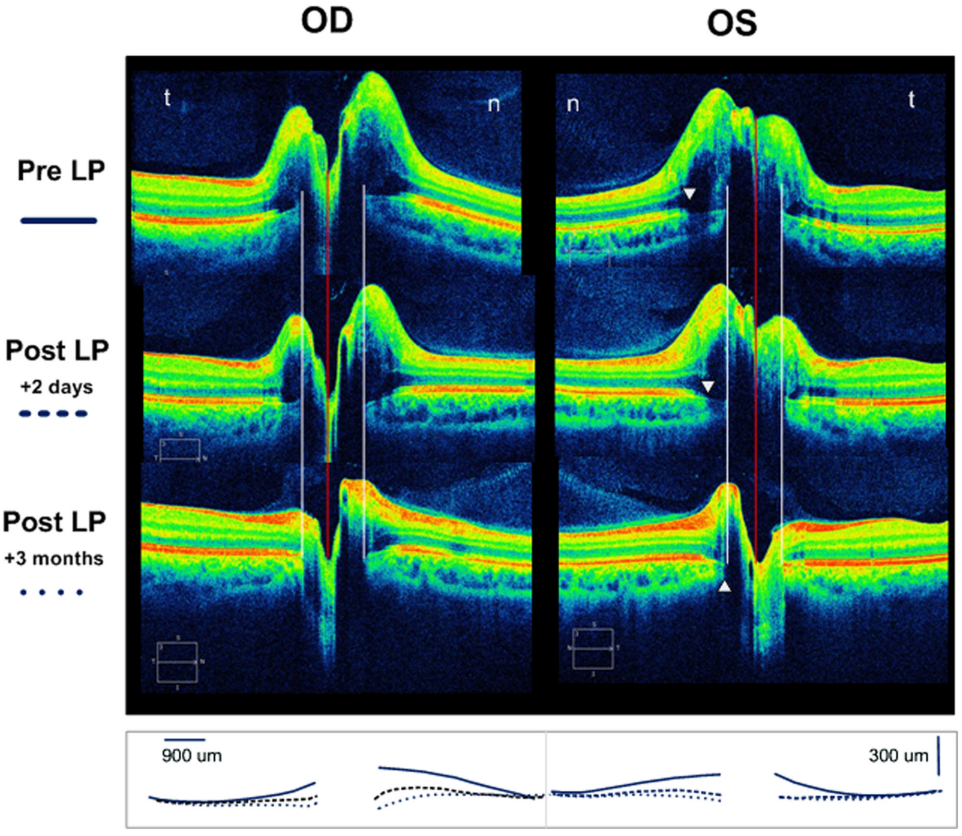

FIGURE 6. The SD-OCT 5-line raster (3:2 aspect ratio) of a 22-year-old man with idiopathic intracranial hypertension (opening pressure, 48 cm) before and after spinal tap and then after 3 months of treatment. Sequential superimposed line tracings of the RPE/BM layer from each raster is summarized in the *bottom row*. The pre-LP SD-OCT shows massive disc elevation in both eyes with anterior displacement of the RPE/BM layer toward the vitreous. Two days later, after the LP, the shape of the RPE/BM becomes flatter and posteriorly displaced OU. There was a corresponding decrease in the RNFL over this time interval (OD, 351 to 283 to 122 μm; OS, 279 to 234 to 112 μm) The RPE/BM bordering the NCO was displaced by at least 150 to 250 μm. *White arrowheads*: the beginning of the penumbra caused by the overlying disc elevation. Although the signal from the margin of the RPE/BM and choroid is diminished, it is still possible to locate the border of the NCO (*white lines*). The NCO diameter is the distance between the *two white lines*. n, nasal; t, temporal; LP, lumbar puncture.

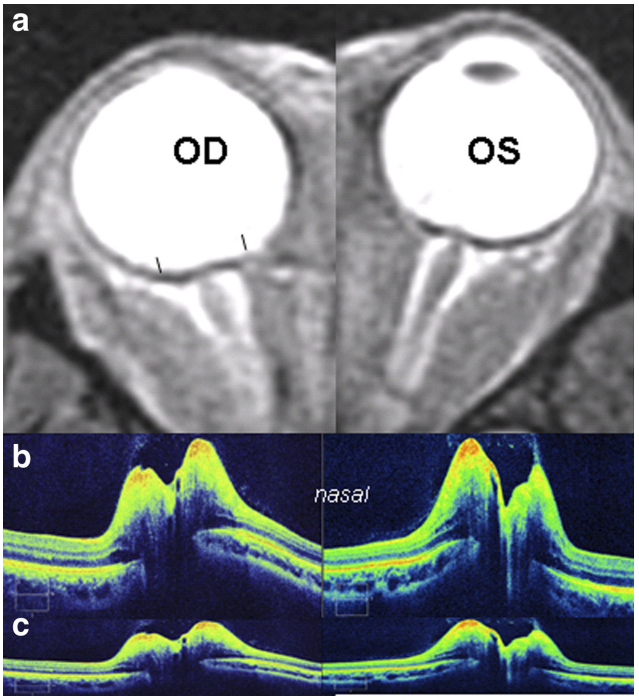

FIGURE 7. A 39-year-old woman with venous sinus thrombosis, papilledema, and opening pressure of 420 mm. Compare the configuration of the RPE/BM layer on SD-OCT (**b**, **c**) to findings on orbital MRI (**a**). The SD-OCT is displayed in the standard aspect ratio of 3:2 (**b**) and in the corrected aspect ratio of 9:2 (**c**). The T2 STIR MRI demonstrates characteristic flattening of the posterior globe with distension of the optic nerve sheath bilaterally. *Black line*: brackets on MRI shows the 9-mm span depicted in the SD-OCT. Note similarities in shape between SD-OCT and MRI.

be mitigated by the simultaneous radial expansion of the scleral canal that pulls the lamina taut. Because the stress and strain in intracranial hypertension is confined to the scleral flange (rather than the entire eye wall), this constraint may be less important in papilledema than it is in glaucoma. This distribution of forces may explain the differences in both the magnitude of displacements, and the sensitivity to translaminar pressure changes in glaucoma and intracranial hypertension.

The findings in this study also suggest that there may be regional differences in the deformation of the peripapillary RPE/BM in subjects with papilledema—that is, a relatively greater deformation of the nasal peripapillary RPE/BM than the temporal region. The explanation for this asymmetric deformation is unknown; we can only speculate on the reasons. However, Downs et al.[48,49] showed that the nasal peripapillary sclera in monkeys is thinner and presumably (though not necessarily) more compliant than the temporal sclera. Using a mathematical model, David et al.[50] suggested that time-dependent shear stress forces increase as the thickness of the eye wall decreases and that these forces are concentrated around the optic nerve. Clinically, the occurrence of spontaneous nasal peripapillary subretinal hemorrhages in crowded tilted myopic discs,[51] flick phosphenes after complete posterior vitreous detachments,[52] and oblique entry of the optic nerve through the NCO all suggest that the nasal region may be more susceptible to deformations due to eye movements, at least. On the other hand the viscoelastic properties of the peripapillary sclera from four quadrants surrounding the optic nerve in both rabbit and monkey show no regional differences in the stress–strain curves.[53]

It has been suggested that the RPE/BM layer located at the NCO or at a fixed distance peripherally may serve as a longitudinal reference plane from which other structural parameters may be derived.[12] Although it is probably true in glaucoma, where the displacements are relatively small and progression is slow, this study showed that in papilledema there can be relatively large, regional deformations of the peripapillary RPE/BM both at the NCO and peripherally over periods of days to weeks. In addition, the deformations may not correlate with the thickening of the overlying RNFL. Moreover, the parallax artifact is problematic in morphometrics that use structural reference points located at different depths. The magnitude of these subsurface deformations in papilledema and SD-OCT artifacts must be considered in disc morphometry in patients with intracranial hypertension.

Using traditional morphometrics, we have shown that slightly more than half the patients with papilledema may exhibit a small inward angular deviation of the RPE/BM.[14] The process of converting the shape data using Procrustes superimposition and the display of shape variables using PCA greatly increases the sensitivity of detecting differences in shape. The PCA in Figure 4 demonstrates that the cluster of PC scores from papilledema showed very little overlap with normal subjects. This indicates that the difference in shape is in fact more common, because nearly all patients with papilledema display some degree of flattening or anterior displacement that is statistically distinguishable from normals, even though this difference in shape may not be obvious by visual inspection of the SD-OCT or MRI.

Burgoyne et al.[54] suggested that the slowing of axoplasmic flow, ischemia, and axonal and glial injury of the optic disc in glaucoma may be influenced, if not caused, by the biomechanical effects of increased pressure on the load-bearing structures (lamina cribrosa and sclera) of the optic nerve head.[54] Histomorphometric studies and in vivo imaging in humans and animal models have demonstrated that an elevation in intraocular pressure can posteriorly displace the optic disc surface, the peripapillary sclera, and the lamina cribrosa.[29,44–46,55–61] In some cases, radial expansion of the scleral canal with consequent stretching of the lamina cribrosa in response to an acute increase in pressure may reduce, if not eliminate, a net posterior displacement of the lamina.[26,47,62] Thickening of the lamina cribrosa, prelaminar neural thickening, late compression, and thinning with failure of the collagen of the lamina and deformation of the neural canal have also been described in experimental glaucoma.[26,46–47,61–64] It is likely that the biomechanical paradigm proposed by these investigators in the study of experimental glaucoma, with some important differences, is also applicable to the changes induced by intracranial hypertension.

It is well known that the margin of a hole in a plate under tension is prone to mechanical failure due to stress concentration at this location. Greene[65] examined the biomechanics of the optic nerve head as a neural portal of the globe that forms a boundary between the intraocular and subarachnoid space. Each compartment, with its own fluid dynamics, maintains an opposing pressure.[66] The relatively high intraocular pressure exerts a compressive force to the eye wall and a tensile expanding force (hoop stress) on the load-bearing structures of the optic nerve (i.e., the peripapillary sclera and lamina cribrosa).[54,67] Contractions of the extraocular muscles with eye movements and blinks may cause transient perturbations in the IOP or directly stress the eye wall itself, especially in the peripapillary sclera.[50–52,65] The intracranial pressure, transmitted through the perioptic subarachnoid compartment compresses the retrolaminar optic nerve and the load-bearing structures, which include the pia.[66] Any change in the magnitude and direction of the translaminar pressure gradient (intraocular pressure minus cerebrospinal fluid pressure) will impose axial and transverse stress and strain across this boundary that may

alter the position, thickness, and shape of the lamina cribrosa and the peripapillary sclera, which in turn may also adversely affect axons, glial cells, and vasculature. The response is also influenced by the material properties of the tissue (i.e., their elasticity and compliance).[30,65–70] This complex interplay between the translaminar pressure differential, the structural geometry, and the biomaterial properties of the optic nerve head may play an important role in a variety of conditions including glaucoma,[54,63,66,71,72] intracranial hypertension, ocular hypotony, and disorders associated with choroidal folds.[35,36]

There are several limitations of this study. The first relates to the relatively small number of patients in any one group. Second, whether the RPE/BM can be used to approximate the deformations of the sclera with intracranial hypertension will ultimately have to be verified, presumably with the development of extended depth imaging or deep penetrating wavelengths in new-generation SD-OCTS. Third, one of the principles of GM is that the placement of semilandmarks should include homologous loci that do not alter positions relative to other semilandmarks. We minimized this effect by excluding subjects with high myopia and positioning the grid parallel to the RPE. Fourth, we emphasized some of the inherent artifacts to consider in any morphometric analysis that uses SD-OCT but especially GM. They include the anatomic distortion induced by the 3:2 aspect ratio, the parallax artifact (correctible by properly orienting the scanning beam), and shadowing of the RPE/BM in disc edema. Finally, this article was confined to a two-dimensional analysis, which is an incomplete description of the peripapillary topography.

Despite these limitations, we suggest that GM is a potentially useful analytical tool for the structural study of the eye. Clinically, examination of the subsurface architecture on the OCT may provide additional information that may aid in the diagnosis and management of patients with disc edema.

References

1. Schuman JS. Spectral domain optical coherence tomography for glaucoma (an AOS thesis). *Trans Am Ophthalmol Soc.* 2008;106:426–458.
2. Schuman JS, Hee MR, Arya AV, et al. Optical coherence tomography: a new tool for glaucoma diagnosis. *Curr Opin Ophthalmol.* 1995;6:89–95.
3. Brusini P, Salvetat ML, Zeppieri M, Tosoni C, Parisi L, Felletti M. Comparison between GDx VCC scanning laser polarimetry and Stratus OCT optical coherence tomography in the diagnosis of chronic glaucoma. *Acta Ophthalmol Scand.* 2006;84:650–655.
4. Mwanza JC, Oakley JD, Budenz DL, Anderson DR. Ability of Cirrus HD-OCT optic nerve head parameters to discriminate normal from glaucomatous eyes. *Ophthalmology.* 2010;118:241–248.
5. Cho JW, Sung KR, Hong JT, Um TW, Kang SY, Kook MS. Detection of glaucoma by spectral domain-scanning laser ophthalmoscopy/optical coherence tomography (SD-SLO/OCT) and time domain optical coherence tomography. *J Glaucoma.* 2010;20:15–20.
6. Frohman E, Costello F, Zivadinov R, et al. Optical coherence tomography in multiple sclerosis. *Lancet Neurol.* 2006;5:853–863.
7. Karam EZ, Hedges TR. Optical coherence tomography of the retinal nerve fibre layer in mild papilloedema and pseudopapilloedema. *Br J Ophthalmol.* 2005;89:294–298.
8. Menke MN, Feke GT, Trempe CL. OCT measurements in patients with optic disc edema. *Invest Ophthalmol Vis Sci.* 2005;46:3807–3811.
9. Ophir A, Karatas M, Ramirez JA, Inzelberg R. OCT and chronic papilledema. *Ophthalmology.* 2005;112:2238.
10. Savini G, Bellusci C, Carbonelli M, et al. Detection and quantification of retinal nerve fiber layer thickness in optic disc edema using stratus OCT. *Arch Ophthalmol.* 2006;124:1111–1117.
11. Scott CJ, Kardon RH, Lee AG, Frisen L, Wall M. Diagnosis and grading of papilledema in patients with raised intracranial pressure using optical coherence tomography vs clinical expert assessment using a clinical staging scale. *Arch Ophthalmol.* 2010;128:705–711.
12. Strouthidis NG, Yang H, Fortune B, Downs JC, Burgoyne CF. Detection of optic nerve head neural canal opening within histomorphometric and spectral domain optical coherence tomography data sets. *Invest Ophthalmol Vis Sci.* 2009;50:214–223.
13. Strouthidis NG, Fortune B, Yang H, Sigal IA, Burgoyne CF. Longitudinal change detected by spectral domain optical coherence tomography in the optic nerve head and peripapillary retina in experimental glaucoma. *Invest Ophthalmol Vis Sci.* 2011;52:1206–1219.
14. Kupersmith MJ, Sibony P, Mandel G, Durbin M, Kardon R. Optical coherence tomography of the swollen optic nerve head: deformation of the peripapillary retinal pigment epithelium layer in papilledema. *Invest Ophthalmol Vis Sci.* 2011;52:6558–6564.
15. Zelditch MLS, DL, Sheets HD, Fink WL. *Geometric Morphometrics for Biologists*: *a Primer*. London: Academic Press; 2004.
16. Adams DC, Rohlf FJ, Slice DE. Geometric morphometrics; ten years of progress following the "revolution". *Italian J Zool.* 2004;71:5–16.
17. Sanfilippo PG, Cardini A, Hewitt AW, Crowston JG, Mackey DA. Optic disc morphology: rethinking shape. *Prog Retin Eye Res.* 2009;28:227–248.
18. Sanfilippo PG, Cardini A, Sigal IA, et al. A geometric morphometric assessment of the optic cup in glaucoma. *Exp Eye Res.* 2010;91:405–414.
19. Rohlf FJ. *Morphometrics at SUNY Stony Brook*. Available at http://life.bio.sunysb.edu/morph/. Accessed September 16, 2011.
20. Sheets HD, Zelditch M, Swiderski D. *Morphometrics Software: IMP-Integrated Morphometrics Package*. Available at: http://www3.canisius.edu/~sheets/morphsoft.html. Accessed September 16, 2011.
21. Bookstein FL. Visualizing group differences in outline shape: methods from biometrics of landmark points. In: Hohne K, Kikinis R, eds. *Visualization in Biomedical Computing. Lecture Notes in Computer Science*: *4th International Conference*, *VBC '96*, *Hamburg*, *Germany*. Berlin: Springer-Verlag; 1996:405–410.
22. Goodall C. Procrustes methods in the statistical analysis of shape. *J R Stat Soc.* 1991;53:285–339.
23. Brodsky MC, Glasier CM. Magnetic resonance visualization of the swollen optic disc in papilledema. *J Neuroophthalmol.* 1995;15:122–124.
24. Brodsky MC, Vaphiades M. Magnetic resonance imaging in pseudotumor cerebri. *Ophthalmology.* 1998;105:1686–1693.
25. Sigal IA, Flanagan JG, Tertinegg I, Ethier CR. Modeling individual-specific human optic nerve head biomechanics: Part I, IOP-induced deformations and influence of geometry. *Biomech Model Mechanobiol.* 2009;8:85–98.
26. Agoumi Y, Sharpe GP, Hutchison DM, Nicolela MT, Artes PH, Chauhan BC. Laminar and prelaminar tissue displacement during intraocular pressure elevation in glaucoma patients and healthy controls. *Ophthalmology.* 2011;118:52–59.
27. Srinivasan VJ, Adler DC, Chen Y, et al. Ultrahigh-speed optical coherence tomography for three-dimensional and en face imaging of the retina and optic nerve head. *Invest Ophthalmol Vis Sci.* 2008;49:5103–5110.
28. Imamura Y, Iida T, Maruko I, Zweifel SA, Spaide RF. Enhanced depth imaging optical coherence tomography of the sclera in dome-shaped macula. *Am J Ophthalmol.* 2011;151:297–302.
29. Morgan WH, Chauhan BC, Yu DY, Cringle SJ, Alder VA, House PH. Optic disc movement with variations in intraocular and cerebrospinal fluid pressure. *Invest Ophthalmol Vis Sci.* 2002;43:3236–3242.
30. Morgan WH, Yu DY, Cooper RL, Alder VA, Cringle SJ, Constable IJ. The influence of cerebrospinal fluid pressure on the lamina cribrosa tissue pressure gradient. *Invest Ophthalmol Vis Sci.* 1995;36:1163–1172.
31. Gass A, Barker GJ, Riordan-Eva P, et al. MRI of the optic nerve in benign intracranial hypertension. *Neuroradiology.* 1996;38:769–773.
32. Sharma M, Volpe NJ, Patel T, Kimmel A. Intracranial hypertension associated with acquired hyperopia and choroidal folds. *Retina.* 1999;19:260–262.

33. Dailey RA, Mills RP, Stimac GK, Shults WT, Kalina RE. The natural history and CT appearance of acquired hyperopia with choroidal folds. *Ophthalmology.* 1986;93:1336–1342.
34. Stimac GK, Mills RP, Dailey RA, Shults WT, Kalina RE. CT of acquired hyperopia with choroidal folds. *AJNR Am J Neuroradiol.* 1987;8:1107–1111.
35. Griebel SR, Kosmorsky GS. Choroidal folds associated with increased intracranial pressure. *Am J Ophthalmol.* 2000;129:513–516.
36. Jacobson DM. Intracranial hypertension and the syndrome of acquired hyperopia with choroidal folds. *J Neuroophthalmol.* 1995; 15:178–185.
37. Sarraf D, Schwartz SD. Bilateral choroidal folds and optic neuropathy: a variant of the crowded disk syndrome? *Ophthalmology.* 2003;110:1047–1052.
38. Westfall AC, Ng JD, Samples JR, Weissman JL. Hypotonus maculopathy: magnetic resonance appearance. *Am J Ophthalmol.* 2004;137:563–566.
39. Taban M, Kosmorsky GS, Singh AD, Sears JE. Choroidal folds secondary to parasellar meningioma. *Eye* (*Lond*). 2007;21:147–150.
40. Madill SA, Connor SE. Computed tomography demonstrates short axial globe length in cases with idiopathic intracranial hypertension. *J Neuroophthalmol.* 2005;25:180–184.
41. Leahey AB, Brucker AJ, Wyszynski RE, Shaman P. Chorioretinal folds: a comparison of unilateral and bilateral cases. *Arch Ophthalmol.* 1993;111:357–359.
42. Cangemi FE, Trempe CL, Walsh JB. Choroidal folds. *Am J Ophthalmol.* 1978;86:380–387.
43. Corbett JJ, Jacobson DM, Mauer RC, Thompson HS. Enlargement of the blind spot caused by papilledema. *Am J Ophthalmol.* 1988; 105:261–265.
44. Yan DB, Coloma FM, Metheetrairut A, Trope GE, Heathcote JG, Ethier CR. Deformation of the lamina cribrosa by elevated intraocular pressure. *Br J Ophthalmol.* 1994;78:643–648.
45. Levy NS, Crapps EE, Bonney RC. Displacement of the optic nerve head: response to acute intraocular pressure elevation in primate eyes. *Arch Ophthalmol.* 1981;99:2166–2174.
46. Bellezza AJ, Rintalan CJ, Thompson HW, Downs JC, Hart RT, Burgoyne CF. Deformation of the lamina cribrosa and anterior scleral canal wall in early experimental glaucoma. *Invest Ophthalmol Vis Sci.* 2003;44:623–637.
47. Yang H, Downs JC, Bellezza A, Thompson H, Burgoyne CF. 3-D histomorphometry of the normal and early glaucomatous monkey optic nerve head: prelaminar neural tissues and cupping. *Invest Ophthalmol Vis Sci.* 2007;48:5068–5084.
48. Downs JC, Blidner RA, Bellezza AJ, Thompson HW, Hart RT, Burgoyne CF. Peripapillary scleral thickness in perfusion-fixed normal monkey eyes. *Invest Ophthalmol Vis Sci.* 2002;43:2229–2235.
49. Downs JC, Ensor ME, Bellezza AJ, Thompson HW, Hart RT, Burgoyne CF. Posterior scleral thickness in perfusion-fixed normal and early-glaucoma monkey eyes. *Invest Ophthalmol Vis Sci.* 2001;42: 3202–3208.
50. David T, Smye S, James T, Dabbs T. Time-dependent stress and displacement of the eye wall tissue of the human eye. *Med Eng Phys.* 1997;19:131–139.
51. Sibony P, Fourman S, Honkanen R, El Baba F. Asymptomatic peripapillary subretinal hemorrhage: a study of 10 cases. *J Neuroophthalmol.* 2008;28:114–119.
52. Enoch JM, Choi SS, Kono M, Schwartz D, Bearse M. Utilization of eye-movement phosphenes to help understand transient strains at the optic disc and nerve in myopia. *Ophthalmic Physiol Opt.* 2003;23:377–381.
53. Downs JC, Suh JK, Thomas KA, Bellezza AJ, Burgoyne CF, Hart RT. Viscoelastic characterization of peripapillary sclera: material properties by quadrant in rabbit and monkey eyes. *J Biomech Eng.* 2003;125:124–131.
54. Burgoyne CF, Downs JC, Bellezza AJ, Suh JK, Hart RT. The optic nerve head as a biomechanical structure: a new paradigm for understanding the role of IOP-related stress and strain in the pathophysiology of glaucomatous optic nerve head damage. *Prog Retin Eye Res.* 2005;24:39–73.
55. Burgoyne CF, Varma R, Quigley HA, Vitale S, Pease ME, Lenane PL. Global and regional detection of induced optic disc change by digitized image analysis. *Arch Ophthalmol.* 1994;112:261–268.
56. Burgoyne CF, Quigley HA, Thompson HW, Vitale S, Varma R. Measurement of optic disc compliance by digitized image analysis in the normal monkey eye. *Ophthalmology.* 1995;102: 1790–1799.
57. Coleman AL, Quigley HA, Vitale S, Dunkelberger G. Displacement of the optic nerve head by acute changes in intraocular pressure in monkey eyes. *Ophthalmology.* 1991;98:35–40.
58. Levy NS, Crapps EE. Displacement of optic nerve head in response to short-term intraocular pressure elevation in human eyes. *Arch Ophthalmol.* 1984;102:782–786.
59. Burgoyne CF, Quigley HA, Thompson HW, Vitale S, Varma R. Early changes in optic disc compliance and surface position in experimental glaucoma. *Ophthalmology.* 1995;102:1800–1809.
60. Yan DB, Flanagan JG, Farra T, Trope GE, Ethier CR. Study of regional deformation of the optic nerve head using scanning laser tomography. *Curr Eye Res.* 1998;17:903–916.
61. Yang H, Thompson H, Roberts MD, Sigal IA, Downs JC, Burgoyne CF. Deformation of the early glaucomatous monkey optic nerve head connective tissue after acute IOP elevation in 3-D histomorphometric reconstructions. *Invest Ophthalmol Vis Sci.* 2011;52: 345–363.
62. Yang H, Downs JC, Sigal IA, Roberts MD, Thompson H, Burgoyne CF. Deformation of the normal monkey optic nerve head connective tissue following acute IOP elevation within 3-D histomorphometric reconstructions. *Invest Ophthalmol Vis Sci.* 2011;52:345–363.
63. Jonas JB, Berenshtein E, Holbach L. Anatomic relationship between lamina cribrosa, intraocular space, and cerebrospinal fluid space. *Invest Ophthalmol Vis Sci.* 2003;44:5189–5195.
64. Downs JC, Yang H, Girkin C, et al. Three-dimensional histomorphometry of the normal and early glaucomatous monkey optic nerve head: neural canal and subarachnoid space architecture. *Invest Ophthalmol Vis Sci.* 2007;48:3195–3208.
65. Greene PR. Mechanical considerations in myopia: relative effects of accommodation, convergence, intraocular pressure and the extraocular muscles. *Am J Optom Physiol Opt.* 1980;57:13.
66. Morgan WH, Yu DY, Balaratnasingam C. The role of cerebrospinal fluid pressure in glaucoma pathophysiology: the dark side of the optic disc. *J Glaucoma.* 2008;17:408–413.
67. Bellezza AJ, Hart RT, Burgoyne CF. The optic nerve head as a biomechanical structure: initial finite element modeling. *Invest Ophthalmol Vis Sci.* 2000;41:2991–3000.
68. Sigal IA, Flanagan JG, Ethier CR. Factors influencing optic nerve head biomechanics. *Invest Ophthalmol Vis Sci.* 2005;46:4189–4199.
69. Sigal IA, Flanagan JG, Tertinegg I, Ethier CR. Finite element modeling of optic nerve head biomechanics. *Invest Ophthalmol Vis Sci.* 2004;45:4378–4387.
70. Sigal IA, Flanagan JG, Tertinegg I, Ethier CR. Modeling individual-specific human optic nerve head biomechanics: Part II, influence of material properties. *Biomech Model Mechanobiol.* 2009;8:99–109.
71. Sigal IA, Roberts MD, Girard M, Burgoyne C, Downs JC. Biomechanical changes of the optic disc. In: Levin LA, Albert DM, eds. *Ocular Disease: Mechanisms and Management*. China: Elsevier; 2010:153–164.
72. Ren R, Jonas JB, Tian G, Zhen Y, Ma K, Li S, et al. Cerebrospinal fluid pressure in glaucoma: a prospective study. *Ophthalmology.* 2010;117:259–266.